nature photonics

Article

https://doi.org/10.1038/s41566-023-01172-6

Sub-picosecond steering of ultrafast incoherent emission from semiconductor metasurfaces

Received: 16 May 2022

Accepted: 8 February 2023

Published online: 20 March 2023

Check for updates

Prasad P. Iyer[1,2] ✉, Nicholas Karl[1], Sadhvikas Addamane[1,2], Sylvain D. Gennaro[1,2], Michael B. Sinclair[1] & Igal Brener[1,2] ✉

The ability to dynamically steer sub-picosecond pulses from a monolithically integrated source is a critical milestone for the fields of nanophotonics and ultrafast optics. Reconfigurable dielectric metasurfaces have demonstrated the potential to exert dynamic control over the properties of light at sub-wavelength scales using spatial phase engineering. However, active manipulation of incoherent light sources remains a challenge, as current phase-sensitive metasurfaces developed for coherent sources cannot be directly applied. Here we theoretically predict and experimentally demonstrate sub-picosecond steering of ultrafast incoherent emission from a light-emitting metasurface over a 70° range. We utilize a monolithic III–V (GaAs) metasurface with embedded (InAs quantum dot) light sources positioned on a reflective Bragg ($AlAs/Al_{0.3}Ga_{0.7}As$) mirror to achieve a large optically induced phase change near the emission wavelength (1.25 μm). We use a spatial light modulator to structure a strong optical pump (800 nm) and project it onto the resonant metasurface to create reconfigurable spatial momentum profiles that dynamically steer the ultrafast (140 fs) quantum dot emission. Such dynamic spatiotemporal control of incoherent sources can enable new technologies for high-speed communications, holography and remote sensing.

The nascent field of reconfigurable metasurfaces—made of optically resonant meta-atoms—has shown great promise in manipulating light–matter interactions through sub-wavelength control of the phase, amplitude and polarization of light[1–5]. These active metasurfaces arbitrarily transform an incident wavefront using a reconfigurable spatial phase profile, but have thus far been limited to manipulating coherent external sources[6–11]. Light-emitting metasurfaces[12] obtained through the integration of incoherent emitters with meta-atoms have been used to statically increase the quantum efficiency of the emission through Purcell factor enhancement[13–15] and control the far-field emission properties[16] of the light to collimate[17] and focus[18] spontaneous emission. Spatiotemporal control at ultrafast timescales of incoherent light emission would represent a substantial technological advancement, allowing low-power light-emitting diodes (LEDs) to replace coherent laser sources, enabling holographic LED displays[19] and other key optical transceiver applications including remote-sensing, perception and high-speed optical communication systems[20,21].

We achieve incoherent emission steering through the imposition of a dynamic spatially structured refractive index profile in the form of a blazed grating on our light-emitting semiconductor metasurface that imparts photonic momentum to the spontaneous emission from embedded epitaxial quantum dots (QDs). The refractive index profile is created using a spatially structured strong optical pump that

[1]Sandia National Laboratories, Albuquerque, NM, USA. [2]Center for Integrated Nanotechnologies, Sandia National Laboratories, Albuquerque, NM, USA. ✉e-mail: ppadma@sandia.gov; ibrener@sandia.gov

https://doi.org/10.1038/s41566-023-01172-6

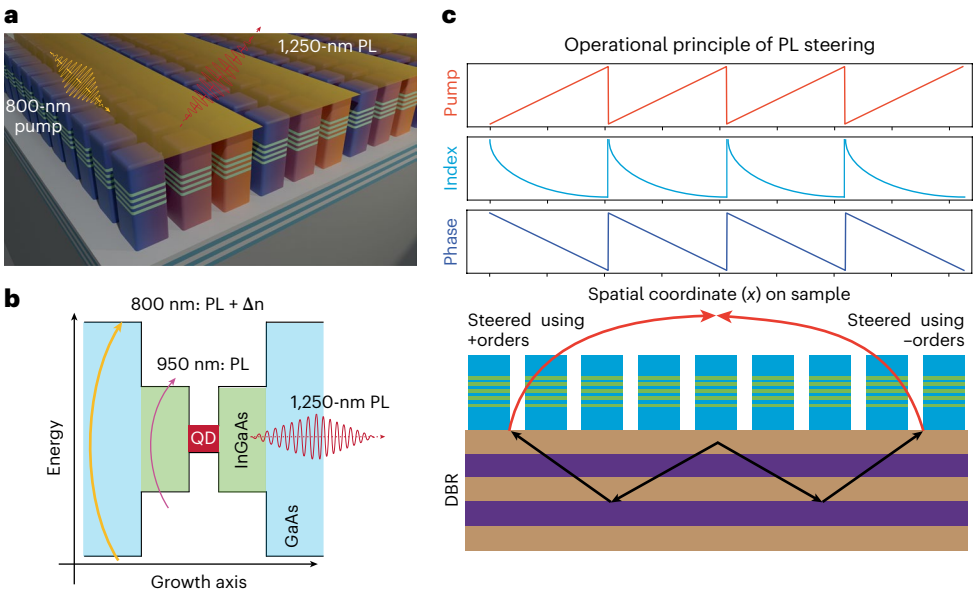

Fig. 1 | Operational principle of incoherent emission steering. a, Schematic of the GaAs metasurface containing InAs QDs embedded inside $In_{0.15}Ga_{0.85}As$ quantum wells grown on a DBR stack using molecular beam epitaxy (MBE) on a GaAs wafer. The schematic shows the spatially structured (800 nm) pump beam (as a yellow periodic gradient) causing a refractive index shift of the resonators, coloured as indigo for low $|\Delta n|$ to orange for high $|\Delta n|$. **b**, Band-structure sketch of the MBE-grown III–V resonators, highlighting the influence of the 800-nm pump (producing an index shift Δn and photoluminescence, PL) and the 950-nm second pump, which only excites the QDs for PL emission. **c**, Operation principle for steering PL from dielectric metasurfaces using structured pumping. The top three panels show the effect of a spatial pump profile on the refractive index and the spatial phase profile of the metasurface. The spatial refractive index grating produces a spatial phase profile inside the resonators, introducing a momentum kick to the PL. Arrows sketch out the possible path of the PL emission from the metasurface to free space, reflecting from the DBR substrate (black arrows). This momentum from the super-imposed meta-grating steers (red arrows) the light emitted from the metasurface.

is reflected off a spatial light modulator (SLM). The spatially varying pump is absorbed by the GaAs resonators to generate a spatially varying free-carrier concentration, which in turn produces a spatially varying refractive index change within the metasurface (Fig. 1a). Combining the structured optical pump with a weaker spatially uniform probe that only excites photoluminescence from the QDs (Fig. 1b), we demonstrate that this reconfigurable meta-grating can induce a momentum shift in the local density of the states (LDOS) to which the QD emission is coupled[17,22]. This, in turn, leads to an angular shift of the spontaneous emission in the far-field (Fig. 1c). Furthermore, we show that the sign of the angular shift is reversed when the blaze of the impressed index grating is reversed. We thus demonstrate that dynamic spatiotemporal control of incoherent light can be achieved using structured materials (dielectric metasurfaces) in combination with a structured optical pump.

Our metasurface design consists of a uniform array of GaAs resonators (Fig. 2a, meta-atoms) with embedded InAs QDs grown on top of a distributed Bragg reflector (DBR). The resonators and metasurface array were designed to maximize the resonant phase change in reflection as a function of the pump intensity, which governs the carrier concentration (Fig. 2b). The geometry of the resonator (height, 670 nm; width, 280 nm) and pitch (400 nm) of the metasurface unit cell were optimized using a differential evolution algorithm operating on the results from finite-difference time-domain (FDTD) simulations (Methods). The figure of merit for the optimization was the magnitude of the phase change at the emission peak of the InAs QDs (λ_e = 1,250 nm) as a function of the optically generated free-carrier concentration within the resonators while maintaining minimal absorption. The low-electron effective mass ($0.06m_e$) of GaAs enables us to produce a large free-carrier-induced refractive-index modulation ($\Delta n \approx 0.5, \Delta\kappa \approx 0.01$ at λ_e, where n and κ represent the real and imaginary parts of the refractive index) with a fluence of 2–3 mJ cm^{-2} at 800 nm (ref. [23]; Supplementary Section 1). The increasing carrier concentration produces nearly 2π phase coverage with less than 30% change in the reflection amplitude and a minimal free-carrier absorption (5–10%) at the emission wavelength (λ_e) at the highest pump intensities in the resonators. The DBR substrate was monolithically grown beneath the resonators to reflect the spontaneous emission of the QDs back into the incident half-space. The DBR consists of alternating layers of $Al_{0.3}Ga_{0.7}As$ (high index) and AlAs (low index) that are lattice-matched to the GaAs substrate. The centre wavelength of the DBR stop band was optimized to occur at 1,225 nm—blueshifted with respect to the peak λ_e of 1,250 nm. The $Al_xGa_{1-x}As$ alloy concentrations were chosen (x_{high} = 0.3 and x_{low} = 1.0) to maximize the index mismatch between the layers of the DBR, while maintaining a bandgap above 800 nm so that absorption of the optical pump occurred only in the resonators. Details of the sample epitaxy and fabrication are provided in Methods. Figure 2c presents the reflection and PL spectra of the fabricated metasurface with peaks at the design wavelength of 1,250 nm. The PL spectra also show the enhancement near the resonant wavelength with a Q-factor of 25.6 ($\lambda_e/\Delta\lambda_{FWHM}$).

To characterize the spatiotemporal dynamics of the PL, we first measured the carrier dynamics at the emission wavelength using transient pump (800 nm)–probe (1,250 nm) spectroscopy (Fig. 2d and Supplementary Section 2) in reflection to show that the carrier lifetime in the metasurface follows an expected bi-exponential decay dynamics[24,25]. The fast component of the reflection decay (τ = 0.54 ps) typically corresponds to the carrier capture time by the QDs[26], and the slow decay (τ of a few picoseconds) corresponds to the lifetime of the carriers (the low-effective-mass electrons) inside the GaAs resonators[25]. Next, the temporal evolution of the incoherent PL was measured in the back focal plane (BFP) of the collection optics using a dual modulation correlation experiment using non-degenerate two-colour-pump excitation. The 800-nm pump (80-fs pulses at a repetition rate of 1 kHz)

https://doi.org/10.1038/s41566-023-01172-6

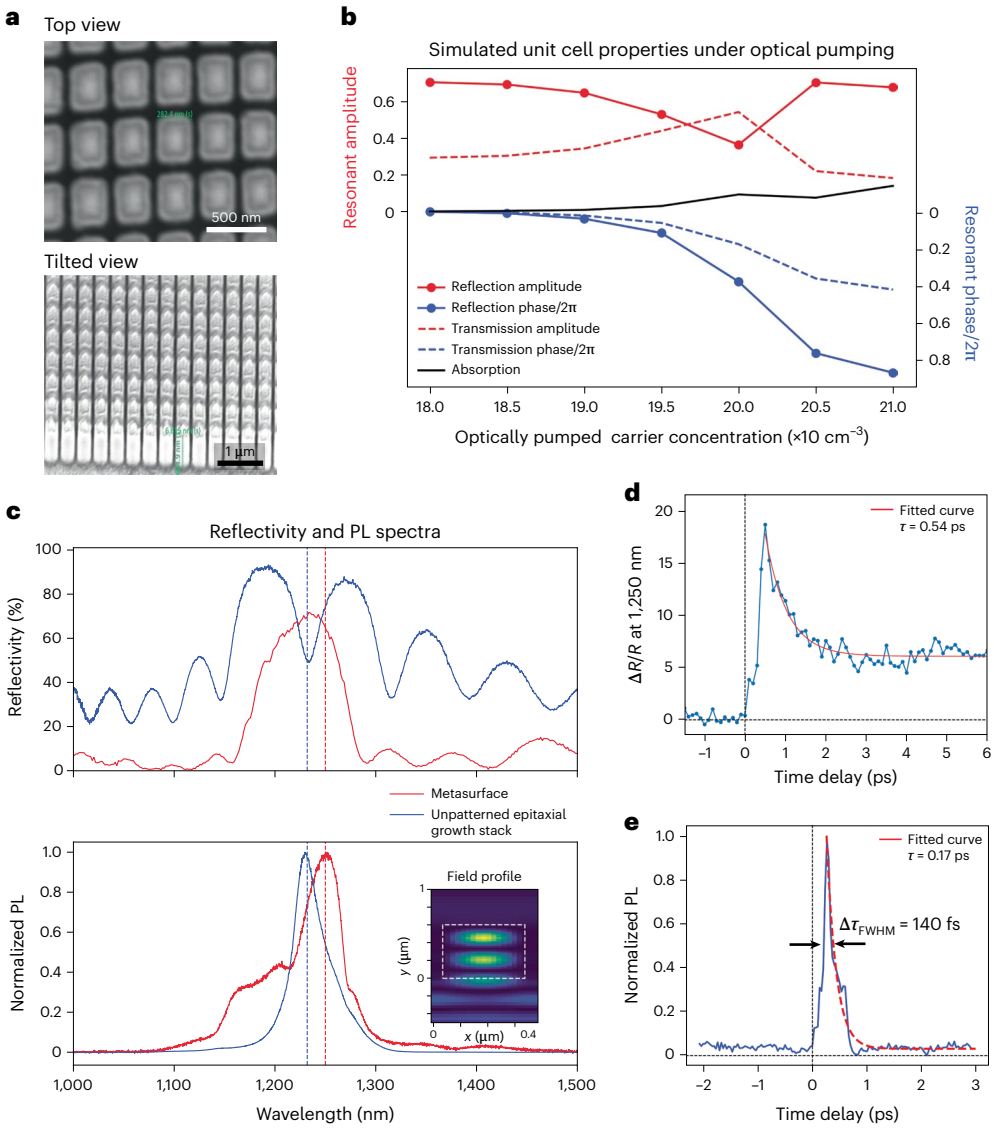

Fig. 2 | Metasurface design and characterization. a, Scanning electron micrographs of the fabricated metasurface showing a top–down view (top; scale bar, 500 nm) and tilted side view (bottom; scale bar, 1 µm). **b**, Simulated unit cell properties of the resonators on the DBR showing nearly 2π phase coverage (blue lines) and high amplitude (red lines) in reflection (solid lines) and transmission (dashed lines). The resonant amplitude is plotted on the left axis (red) and the phase on the right axis (blue). The black solid line shows the increased absorption in the system as a function of the optically pumped free carriers. **c**, Measured reflectivity (top) and PL (bottom) spectra of the metasurface (red curve) and the bare grown wafer (blue curve). The coloured dashed lines represent the PL peak wavelengths for the metasurface (red) and the as-grown wafer (blue) in both panels. The inset colour plot represents the resonant magnetic field profile of the metasurface unit cell, with the white dashed line denoting the outline of the GaAs resonator. **d**, Transient time-domain reflectivity change ($\Delta R/R$) of the metasurface at 1,250 nm as a function of the pump (800 nm)–probe (1,250 nm) delay. The red curve is an exponential decay fit demonstrating the fast (0.54 ps) decay time constant associated with QD relaxation. **e**, Temporal PL signature using a dual modulated (5/7) pump–probe architecture (Methods and Supplementary Fig. 2) locked in at the sum frequency signal from the metasurface, showing a decay constant of 170 fs (red dashed fitted curve) and pulse width of 140 fs (FWHM).

introduces the spatially varying free-carrier profile and excites the QDs (Fig. 1b), whereas the spatially uniform pump at 950 nm is at a much lower fluence (1 µJ cm^{-2}, 100 fs at a repetition rate of 1 kHz) and only excites the electronic transitions of the QDs (Fig. 1b), without leading to a free-carrier-induced index change. This two-colour PL correlation technique has been used extensively in the past to study the PL lifetimes[27–30] of various materials (see Methods for a more detailed explanation). The ultrafast absorption dynamics from self-assembled InAs QDs in $In_{0.15}Ga_{0.85}As$ quantum wells grown on a DBR stack have been measured previously and have been used as the basis for QD-saturable absorbers for external cavity lasers[31–35]. These sub-picosecond transitions have been attributed to thermionic hole activation in passive QD structures at high pump powers in transient transmission and absorption measurements[31,34]. Here we exploit those same transitions to rapidly turn on (limited by carrier capture time) and turn off (hole activation) the emission from the QDs to result in PL pulses with a measured temporal FWHM (full-width at half-maximum) of 140 fs (Fig. 2e)[35–37].

Unidirectional steering of PL is demonstrated using momentum-resolved temporal measurements for different spatial patterns applied to the 800-nm pump beam using the SLM. In particular, the pump beam is structured using a spatial intensity profile corresponding to

https://doi.org/10.1038/s41566-023-01172-6

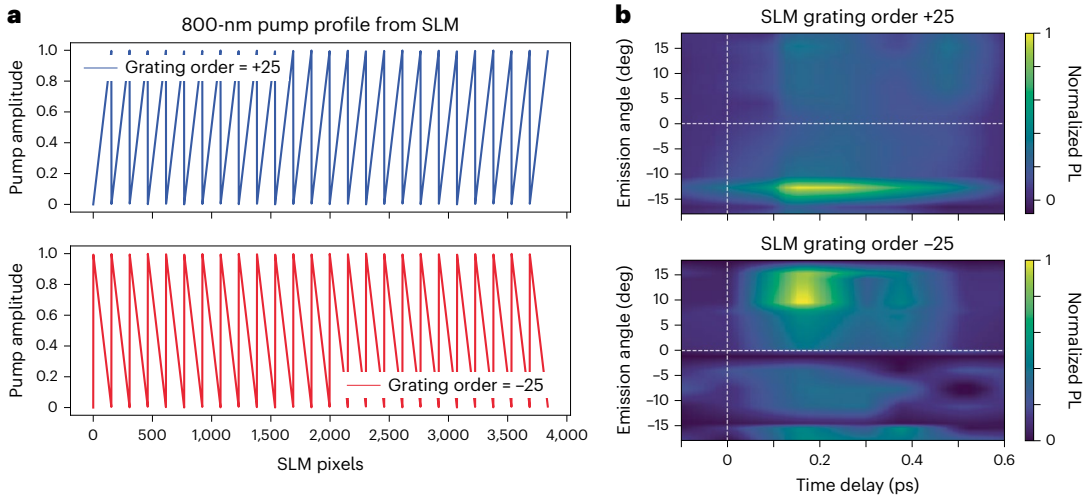

Fig. 3 | Spatiotemporal control of light emission. a, Designed spatial amplitude profile of the 800-nm pump beam encoded using the SLM. The top panel shows the designed pump profile for a positive blazed grating (order = +25), and the bottom panel shows the amplitude for a negative blazed grating (order = −25). These pump profiles are imaged onto the sample to create a spatial refractive index grating. **b**, Momentum-resolved temporal evolution of the PL from InAs QDs, measured as a function of the delay between the 950-nm pump and 800-nm pump. The top panel shows the temporal evolution of the PL for a +25-grating order profile of the 800-nm pump (Fig. 3a), and the bottom panel shows the BFP PL evolution for a −25-grating order.

a blazed grating (with positive and negative slopes). We characterize the blazed grating of the pump beam by its 'order', which corresponds to the number of periods across the SLM width. The pump beam is demagnified and imaged onto the ~300-μm^2 metasurface sample (Fig. 3a). The periodicity of the resonator array[36,37] is designed such that the intrinsic emission directions are away from normal along ±35°, and are then steered towards the normal using the pump-induced meta-grating. As mentioned above, the structured pump illumination induces a dynamic spatial phase profile that superimposes a reconfigurable meta-grating on the sample. In Fig. 3 we report that, for a blazed grating profile of order 25, the far-field emission angle of the PL changes depending on the sign of the slope of the grating profile. The positive-sloped grating steers the emission lobe from −35° towards −16°, and the negative-sloped grating steers the emission lobe at +35° towards +16° (Fig. 3b). The asymmetry in the angular bandwidth of the emission lobes between the top and bottom panels is due to the limits of the angular measurements and the aberrations in the time-resolved measurements while imaging the BFP (Supplementary Section 7). The onset of the steering follows the rising edge of the pump, and the dual modulation, non-degenerate two-colour pump experiment tracks the temporal decay of the PL. The observed temporal evolution of the PL, shifting to opposite angular directions for positive and negative blaze directions, demonstrates that we can steer the incoherent PL into different directions at femtosecond timescales using different pump patterns.

Next, we demonstrate that the PL can be unidirectionally steered over a 70° field of view (limited by the optics in the set-up) based on the grating order imposed on the 800-nm optical pump. The intrinsic emission directions are defined by the local density of states (LDOS) of the unpumped (or uniformly pumped) metasurface and correspond to two PL lobes (Fig. 4a, middle panel) at symmetric directions away from the normal (0°) at ±35°. The momentum of the spatially blazed pump dynamically modifies the LDOS[17,22], which results in an angular shift in the intrinsic emission pattern.

The momentum of a positively sloped pump meta-grating steers the lobe from −35° towards normal, while the negatively sloped meta-grating steers the lobe intrinsically emitting at +35° towards normal. We model the normalized far-field emission momentum, $\mathbf{k}_F$, based on momentum conservation principles: $\mathbf{k}_F = \mathbf{k}_I + \mathbf{k}_p$, where $\mathbf{k}_I$ is the intrinsic emission momentum of the metasurface and $\mathbf{k}_p$ is the pump-induced grating momentum. The final emission angle is calculated using $\sin(\theta_F) = k_F/k_0$, where $k_0 = 2\pi/\lambda_e$ (Supplementary Section 3). In Fig. 4b we plot the measured PL in the BFP normalized per SLM pattern (Supplementary Section 3) at a fixed time delay of 150 fs and overlay the results of our analytic model (dashed black lines). This momentum conservation model closely matches the measured steering, giving us the ability to analytically predict the PL steering angle from the metasurface for a given pump grating order. We also verified that the unpatterned epitaxial wafer (Supplementary Section 4) does not measurably steer the PL under the same pumping conditions to demonstrate that this phenomenon is possible only with the resonant phase shift enhancements enabled by the dielectric metasurface.

In conclusion, we have demonstrated that incoherent PL can be dynamically steered at ultrafast timescales using a reconfigurable semiconductor metasurface. A grating-like intensity profile of the optical pump leads to a spatial refractive index profile on the metasurface that dynamically steers the far-field PL from the QDs embedded in the meta-atoms. We have leveraged the ultrafast QD transitions to generate a 140-fs (FWHM) PL pulse that directly translates into micrometre-scale depth resolution for time-of-flight[38] remote sensing applications. This monolithic III–V metasurface architecture forms an ideal platform to generate dynamically reconfigurable emission patterns given the low-loss free-carrier-dependent index change enabled by GaAs and the ultrafast transitions of the InAs QDs. Such a source opens a new technology space where incoherent sources replace lasers while retaining the ability to be dynamically steerable over a wide field of view. The demonstrated architecture forms a proof of concept to develop an electrically driven luminescent device where the resonant spatial phase profiles can be achieved using known index modulation methods[4,9,10,39–43]. These solid-state, integrated, ultrafast dynamically steerable sources are not only extremely useful in the technologically important near-infrared bandwidth, but can be extended to other visible and mid-infrared wavelengths. Ultimately, we have demonstrated here that spatiotemporal control over incoherent light emission, previously considered impossible, is indeed possible using dynamic momentum-matched reconfigurable semiconductor meta-gratings.

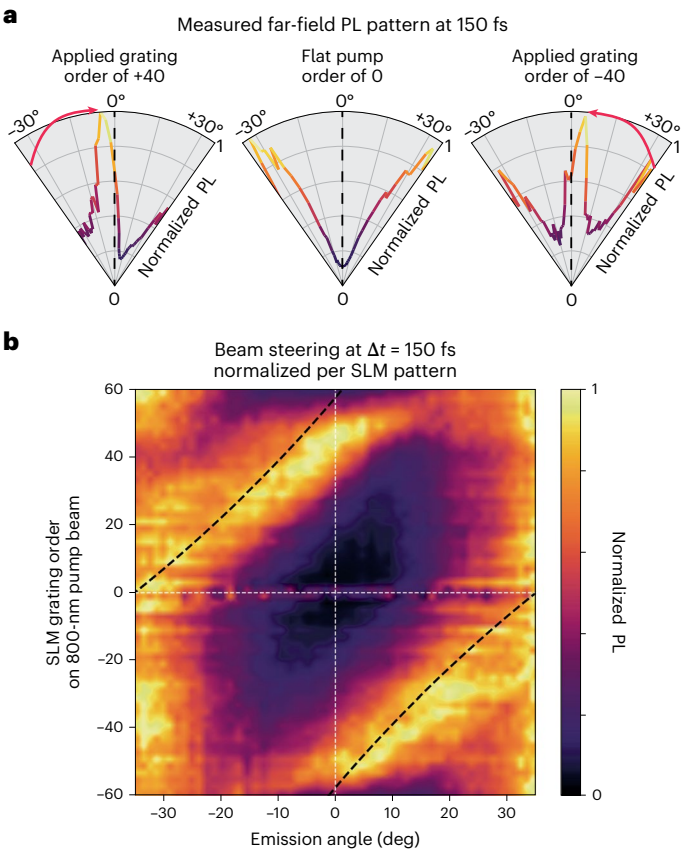

Fig. 4 | Beam-steering of PL. a, Measured far-field radiation polar plots of the PL at 150-fs delay between the pump and probe for different applied grating order patterns at +40, 0 (flat pump) and −40. The red arrows indicate the direction of steering of intrinsic lobes towards the normal (0°). **b**, PL steering demonstrated in the BFP as a function of different pump grating profiles at T_0 + 150 fs. The positive grating orders steer the light from −35° to 0°, and the negative grating orders take the emitted light from +35° to 0°.

Online content

Any methods, additional references, Nature Portfolio reporting summaries, source data, extended data, supplementary information, acknowledgements, peer review information; details of author contributions and competing interests; and statements of data and code availability are available at https://doi.org/10.1038/s41566-023-01172-6.

References

1. Arbabi, E. et al. MEMS-tunable dielectric metasurface lens. *Nat. Commun.* **9**, 812 (2018).
2. Huang, Y.-W. et al. Gate-tunable conducting oxide metasurfaces. *Nano Lett.* **16**, 5319–5325 (2016).
3. Butakov, N. A. et al. Broadband electrically tunable dielectric resonators using metal-insulator transitions. *ACS Photonics* **5**, 4056–4060 (2018).
4. Iyer, P. P. et al. III-V heterojunction platform for electrically reconfigurable dielectric metasurfaces. *ACS Photonics* **6**, 1345–1350 (2019).
5. Yao, Y. et al. Electrically tunable metasurface perfect absorbers for ultra-thin mid-infrared optical modulators. *Nano Lett.* **14**, 6526–6532 (2014).
6. Xie, Y.-Y. Metasurface-integrated vertical cavity surface-emitting lasers for programmable directional lasing emissions. *Nat. Nanotechnol.* **15**, 125–130 (2020).
7. Shaltout, A. Spatiotemporal light control with frequency-gradient metasurfaces. *Science* **365**, 374–377 (2019).
8. Klopfer, E. et.al. High-quality-factor silicon-on-lithium niobate metasurfaces for electro-optically reconfigurable wavefront shaping. *Nano Lett.* https://doi.org/10.1021/ACS.NANOLETT.1C04723 (2021).
9. Thureja, P. et al. Array-level inverse design of beam steering active metasurfaces. *ACS Nano* **14**, 15042–15055 (2020).
10. Wu, P. C. et al. Dynamic beam steering with all-dielectric electro-optic III–V multiple-quantum-well metasurfaces. *Nat. Commun.* **10**, 3654 (2019).
11. Park, J. et al. All-solid-state spatial light modulator with independent phase and amplitude control for three-dimensional LiDAR applications. *Nat. Nanotechnol.* **16**, 69–76 (2020).
12. Vaskin, A. et al. Light-emitting metasurfaces. *Nanophotonics* **8**, 1151–1198 (2019).
13. Liu, S. et al. Light-emitting metasurfaces: simultaneous control of spontaneous emission and far-field radiation. *Nano Lett.* **18**, 6906–6914 (2018).
14. Staude, I. et al. Shaping photoluminescence spectra with magnetoelectric resonances in all-dielectric nanoparticles. *ACS Photonics* **2**, 172–177 (2015).
15. Yuan, L. et al. Manipulation of exciton dynamics in single-layer WSe_2 using a toroidal dielectric metasurface. *Nano Lett.* **21**, 9930–9938 (2021).
16. Khaidarov, E. et al. Control of LED emission with functional dielectric metasurfaces. *Laser Photon. Rev.* **14**, 1900235 (2020).
17. Iyer, P. P. et al. Unidirectional luminescence from InGaN/GaN quantum-well metasurfaces. *Nat. Photon.* **14**, 543–548 (2020).
18. Mohtashami, Y. et al. Light-emitting metalenses and meta-axicons for focusing and beaming of spontaneous emission. *Nat. Commun.* **12**, 3591 (2021).
19. Song, W. et al. 3D holographic displays: large-scale Huygens' metasurfaces for holographic 3D near-eye displays. *Laser Photon. Rev.* **15**, 2170047 (2021).
20. Kim, I. et al. Nanophotonics for light detection and ranging technology. *Nat. Nanotechnol.* **16**, 508–524 (2021).
21. Akselrod, G. M. et al. Lidar systems based on tunable optical metasurfaces. US patent 20210141060 (2021).
22. Langguth, L. et al. Plasmonic phase-gradient metasurface for spontaneous emission control. *Phys. Rev. B* **92**, 205401 (2015).
23. Karl, N. et al. Frequency conversion in a time-variant dielectric metasurface. *Nano Lett.* **20**, 7052–7058 (2020).
24. Maas, H. C. D. J. et al. Growth parameter optimization for fast quantum dot SESAMs. *Opt. Express* **16**, 18646–18656 (2008).
25. Addamane, S. J. et al. Submonolayer quantum-dot based saturable absorber for femtosecond pulse generation. *J. Electron. Mater.* **50**, 2710–2715 (2021).
26. Stintz, A. et al. Ultrafast carrier-relaxation dynamics in self-assembled InAs/GaAs quantum dots. *JOSA B* **19**, 1480–1484 (2002).
27. Brener, I. et al. Decay times of excitons in lattice-matched InGaAs/InP single quantum wells. *Appl. Phys. Lett.* **58**, 965 (1998).
28. O'Driscoll, I. et al. Electron and hole dynamics of InAs/GaAs quantum dot semiconductor optical amplifiers. *Appl. Phys. Lett.* **91**, 071111 (2007).
29. Quochi, F. et al. Coulomb and carrier-activation dynamics of resonantly excited InAs/GaAs quantum dots in two-color pump-probe experiments. *Phys. Rev. B* **67**, 235323 (2003).
30. Sjodin, T. et al. Ultrafast carrier dynamics in silicon: a two-color transient reflection grating study on a (111) surface. *Phys. Rev. Lett.* **81**, 5664–5667 (1998).

31. Rafailov, E. U. et al. Fast quantum-dot saturable absorber for passive mode-locking of solid-state lasers. *IEEE Photonics Technol. Lett.* **16**, 2439–2441 (2004).
32. Bellancourt, A. R. et al. Modelocked integrated external-cavity surface emitting laser. *IET Optelectron.* **3**, 61–72 (2009).
33. Maas, D. J. H. C. et al. Recombination dynamics in quantum dot semiconductor 1 saturable absorber mirrors (QD-SESAMs). In *Proc. 2008 Conference on Quantum Electronics and Laser Science Conference on Lasers and Electro-Optics, CLEO/QELS* (Optical Society of America, 2008); https://doi.org/10.1109/CLEO.2008.4551066
34. Quochi, F. et al. Ultrafast carrier dynamics of resonantly excited 1.3-μm InAs/GaAs self-assembled quantum dots. *Phys. B* **314**, 263–267 (2002).
35. Lagatsky, A. A. et al. Ultrashort-pulse lasers passively mode locked by quantum-dot-based saturable absorbers. *Prog. Quantum Electron.* **34**, 1–45 (2010).
36. van Dam, D. et al. Directional and polarized emission from nanowire arrays. *Nano Lett.* **15**, 4557–4563 (2015).
37. Diedenhofen, S. L. et al. Controlling the directional emission of light by periodic arrays of heterostructured semiconductor nanowires. *ACS Nano* **5**, 5830–5837 (2011).
38. Na, Y. et al. Ultrafast, sub-nanometre-precision and multifunctional time-of-flight detection. *Nat. Photon.* **14**, 355–360 (2020).
39. Kafaie Shirmanesh, G., Sokhoyan, R., Pala, R. A. & Atwater, H. A. Dual-gated active metasurface at 1,550 nm with wide (>300°) phase tunability. *Nano Lett.* **18**, 2957–2963 (2018).
40. Li, S. Q. et al. Phase-only transmissive spatial light modulator based on tunable dielectric metasurface. *Science* **364**, 1087–1090 (2019).
41. Abdollahramezani, S. et al. Electrically driven programmable phase-change meta-switch reaching 80% efficiency. *Nat. Commun.* **13**, 1696 (2022).
42. Wang, Y. et al. Electrical tuning of phase-change antennas and metasurfaces. *Nat. Nanotechnol.* **16**, 667–672 (2021).
43. Zhang, Y. et al. Electrically reconfigurable non-volatile metasurface using low-loss optical phase-change material. *Nat. Nanotechnol.* **16**, 661–666 (2021).

Methods

FDTD simulation set-up

Lumerical FDTD[44] was used to model the scattering (S_{11} and S_{22}) properties of the unit cell of a GaAs resonator placed on a reflective DBR substrate. The design parameters of height and width of the resonator, pitch of the metasurface and the centre wavelength of the DBR stack were optimized using generic algorithms (differential evolution in Scipy[45]) to maximize the phase shift and reflection coefficients at the emission wavelength of the InAs QDs (1,250 nm) while minimizing the free-carrier absorption in the resonators. Please note that the InAs QDs were not included in the design simulations as they are considered perturbative light emitters embedded within the resonators. The 'grating s-params' object was used in Lumerical to simulate the amplitude and phase response of unit cells of different dimensions, which consist of a plane wave (TE-polarized) source, field and power monitors to estimate the far-field complex reflection and transmission coefficients. The propagation-dependent phase accumulation was subtracted from the final figure of merit, which maximized the phase shift as a function of free carriers present in the GaAs resonator. The Drude-model-based free-carrier refraction was used to predict the refractive index of GaAs (Supplementary Section 1). Refractive-index values were taken from previously validated models[23] (for GaAs at 3.5, $Al_{0.3}Ga_{0.7}As$ at 3.2 and AlAs at 2.98 for an operating wavelength of 1,250 nm).

Semiconductor growth

The wafer was grown on an undoped GaAs substrate using MBE. The GaAs substrate was first degassed at 630 °C for 10 min under an arsenic overpressure. The growth sequence started with a 150-nm GaAs buffer layer (600 °C), followed by a DBR consisting of 15 pairs of AlAs/$Al_{0.3}Ga_{0.7}As$ with thickness of $\lambda/4n$. The QDs were grown embedded in an ~0.5-μm GaAs membrane on top of the DBR. The QDs were grown at 490 °C as dots-in-a-well (DWELL) regions with InAs QDs embedded in asymmetric $In_{0.15}Ga_{0.85}As$ quantum wells. Reflection high-energy electron diffraction was used to confirm the crystalline features during initial GaAs growth and to confirm the formation of QDs. The growth temperature was monitored using a pyrometer.

Fabrication process flow

The metasurface design was written on the MBE-grown samples using electron-beam lithography (JEOL JBX-6300FS) with ZEP520a[46] resist using a writing dose of 225 μC cm^{-2}. The resist was spun onto the sample at 3,000 r.p.m. in 30 s and baked at 170 °C for 5 min. After writing the patterns using electron-beam lithography, the resist was developed with *n*-amyl acetate for 90 s. The ZEP520a resist was used as a mask to dry-etch into the GaAs layers to form the metasurface resonators using reactive ion etching (Cl_2, BCl_3, Ar and N_2-based recipe) tool with laser endpoint detection to stop the etch before the DBR stack. The ZEP520a resist was finally removed after the etching process using *N*-methyl pyrrolidone solvent at 80 °C for 1 h.

Measurement set-up details

Reflection spectrum. The near-infrared reflection spectra were measured using a white-light source (stabilized tungsten halogen lamp) to illuminate the sample through a 50-mm plano-convex lens. The reflected light was captured and directed into an InGaAs Peltier-cooled spectrometer (NIR Quest 512 from Ocean Optics) to measure the signal between 900 nm and 1,500 nm. The measured spectrum from the metasurface was normalized to the spectrum measured from a gold sample as the reference, with the dark noise in the spectrometer subtracted from both spectra.

PL spectrum. The metasurface samples were pumped using a laser diode at 808 nm (Thorlabs, L808P200) with an operating current of 50 mA in the laser driver. The emission from the sample was directed to a liquid-nitrogen-cooled InGaAs camera attached to an Acton 2500I spectrometer using a blazed grating (900 g mm^{-1}) centred at 1,200 nm. The signal was integrated for 1 s, and the dark noise in the detector was subtracted from the measured PL spectra. The continuous-wave pump PL measurement was used to estimate the spectral bandwidth of light emission from the resonant metasurface. The spectra from the metasurfaces and the unpatterned epitaxial films (Fig. 2) were independently normalized to avoid comparisons of emission efficiency.

Momentum-resolved temporal PL. The ultrafast two-colour pump experiment was carried out using a Ti:sapphire amplifier at 800 nm (Astrella, Coherent) and an optical parametric amplifier that produced a signal and idler beam. The 800-nm beam was split into two, with one of the beams sourcing the optical parametric amplifier and the other pumping the sample after going through a piezoelectric delay stage (Newport) and reflecting from an SLM (Thorlabs Exulus-4K UHD). The idler beam (1,900 nm) was frequency-doubled using a BBO crystal to generate a 950-nm beam to resonantly excite the InAs QDs in the metasurface. The 800-nm beam size was matched to the aperture of the SLM (143 mm^2) and was then reduced in size to match the size of the metasurface (300 μm^2) by using a two-stage telescope with four achromatic doublet lenses (f = 145 mm, 45 mm, 200 mm and 12 mm). The final objective lens collecting the PL from the metasurface was a high-NA (0.83), near-infrared coated aspheric lens with a diameter of 25 mm. The BFP of this objective lens was imaged onto a femtowatt InGaAs detector in reflection using a telescope with a magnification of 2.2 (f = 250 mm and 150 mm). The detector was also placed on a piezoelectric translation stage (Newport) and measurements carried out using a lock-in amplifier (SRS 830). The 800-nm and 950-nm pump beams were chopped by the same fan with dual holes, with an 800-nm beam going through the outer holes and the 950-nm beam chopped by the inner holes at relatively prime (5/7) frequencies. The lock-in amplifier was fed the sum frequency of these holes as the reference. The 800-nm and 950-nm pumps were combined before the final objective lens using an 830-nm long-pass dichroic filter placed at 45°. The femtowatt detector had an iris with a diameter of 100 μm in front of it, along with two long-pass filters at 1,064 nm and 1,150 nm in addition to the 1,000-nm (short pass) dichroic filter, to prevent any of the pumps from directly hitting the detector.

Data availability

All data generated or analysed during this study are included in this published Article (and its Supplementary Information files).

References

44. *FDTD Solutions* (Lumerical Solutions, 2021); https://www.ansys.com/products/photonics/fdtd
45. Storn, R. & Price, K. Differential evolution—a simple and efficient heuristic for global optimization over continuous spaces. *J. Glob. Optim.* **11**, 341–359 (1997).
46. Kawasaki-shi, K. et al. *ZEP520A. High Resolution Positive Electron Beam Resist*. Technical Report (Zeon, Specialty Materials Division, 2003).

Acknowledgements

This work was supported by the US Department of Energy (DOE), Office of Basic Energy Sciences, Division of Materials Sciences and Engineering and performed, in part, at the Center for Integrated Nanotechnologies, an Office of Science User Facility operated for the US DOE Office of Science. Sandia National Laboratories is a multi-mission laboratory managed and operated by National Technology and Engineering Solutions of Sandia, LLC, a wholly owned subsidiary of Honeywell International, Inc., for the US DOE's National Nuclear Security Administration under contract no. DE-NA0003525. This Article describes objective technical results and analysis. Any subjective views or opinions that might be expressed in the paper do

not necessarily represent the views of the US DOE or the United States Government. This study was funded by the US DOE Basic Energy Science Program (BES20017574).

Author contributions

P.P.I., N.K. and I.B. designed the study. P.P.I. performed the numerical simulations and fabricated the device. S.A. grew the support wafer in MBE. P.P.I., N.K. and S.D.G. measured the ultrafast results. P.P.I. wrote the paper with input from all the authors under the supervision of M.B.S. and I.B.

Competing interests

The authors declare no competing interests.

Additional information

Supplementary information The online version contains supplementary material available at https://doi.org/10.1038/s41566-023-01172-6.

Correspondence and requests for materials should be addressed to Prasad P. Iyer or Igal Brener.

Peer review information *Nature Photonics* thanks the anonymous reviewers for their contribution to the peer review of this work.